International Journal of Applied Earth Observation and Geoinformation 13 (2011) 265–276

Contents lists available at ScienceDirect

International Journal of Applied Earth Observation and Geoinformation

journal homepage: www.elsevier.com/locate/jag

Estimating land-surface temperature under clouds using MSG/SEVIRI observations

Lei Lu[a,b,c,*], Valentijn Venus[b], Andrew Skidmore[b], Tiejun Wang[b], Geping Luo[a]

[a] Xinjiang Institute of Ecology and Geography, CAS, 818 South Beijing Road, 830011 Urumqi, China
[b] International Institute for Geo-information Science and Earth Observation (ITC), Hengelosestraat 99, 7500 AA Enschede, The Netherlands
[c] Graduate University of Chinese Academy of Sciences, 19A YuQuan Rd, 100049 Beijing, China

ARTICLE INFO

Article history:
Received 12 September 2009
Accepted 23 December 2010

Keywords:
Land-surface temperature (LST)
LST under clouds
4-Channel algorithm
Heliosat-2 algorithm
Temporal neighboring-pixel approach

ABSTRACT

The retrieval of land-surface temperature (LST) from thermal infrared satellite sensor observations is known to suffer from cloud contamination. Hence few studies focus on LST retrieval under cloudy conditions. In this paper a temporal neighboring-pixel approach is presented that reconstructs the diurnal cycle of LST by exploiting the temporal domain offered by geo-stationary satellite observations (i.e. MSG/SEVIRI), and yields LST estimates even for overcast moments when satellite sensor can only record cloud-top temperatures. Contrasting to the neighboring pixel approach as presented by Jin and Dickinson (2002), our approach naturally satisfies all sorts of spatial homogeneity assumptions and is hence more suited for earth surfaces characterized by scattered land-use practices. Validation is performed against *in situ* measurements of infrared land-surface temperature obtained at two validation sites in Africa. Results vary and show a bias of −3.68 K and a RMSE of 5.55 K for the validation site in Kenya, while results obtained over the site in Burkina Faso are more encouraging with a bias of 0.37 K and RMSE of 5.11 K. Error analysis reveals that uncertainty of the estimation of cloudy sky LST is attributed to errors in estimation of the underlying clear sky LST, all-sky global radiation, and inaccuracies inherent to the 'neighboring pixel' scheme itself. An error propagation model applied for the proposed temporal neighboring-pixel approach reveals that the absolute error of the obtained cloudy sky LST is less than 1.5 K in the best case scenario, and the uncertainty increases linearly with the absolute error of clear sky LST. Despite this uncertainty, the proposed method is practical for retrieving the LST under a cloudy sky condition, and it is promising to reconstruct diurnal LST cycles from geo-stationary satellite observations.

1. Introduction

Land-surface temperature (LST) is not only a key element that affects the mass, energy, and momentum exchanges between biosphere and atmosphere, but also an important variable in studies of weather, climate, environment, ecology, and resource management (Jin and Dickinson, 2002; Kearney and Porter, 2004; Mallick et al., 2007). The requirements of LST accuracy and scale may differ among various applications. For instance, to obtain an overall accuracy of $\pm 50\ W\ m^{-2}$ on instantaneous heat fluxes or ±0.8 mm/day on water evaporation at field scale, an accuracy of LST between 0.5 K and 1.0 K is required (Seguin et al., 1999). The same accuracy of LST is also required in retrieval of soil moisture content (SMC) using the thermal inertia approach (Verstraeten et al., 2006). On the global scale, accuracies of 2 K are acceptable (Jin and Dickinson, 2002).

Remote sensing is an effective tool to provide LST observations at regional and global scale. Remote sensors with infrared channels, such as the Advanced Very High Resolution Radiometer (AVHRR) and the Moderate-Resolution Imaging Spectrometer (MODIS), have been playing an important role in estimating LST. In the past decades, a few algorithms have been developed to estimate LST with the aim to achieve an accuracy ranging between 0.8 and 1 K. These algorithms rely on methods that use the available information according to the spectral, directional and temporal features of the considered sensors. For example, the widely accepted algorithm TES (Temperature Emissivity Separation) (Gillespie et al., 1998) was developed for the spectral features of ASTER (Advanced Space Thermal Emission and Reflection Radiometer), which yields single temporal and mono-directional observations within several spectral bands in the thermal infrared domain. Restricted by the available channels of some sensors such as Landsat TM, researchers focused on algorithms that retrieve LST using one thermal band only, like the mono-window algorithm developed by Qin et al. (2001) and those proposed by Jiménez-Muñoz and Sobrino (2003). For sensors with multi-channels in TIR (thermal infrared) spectrum,

* Corresponding author at: Xinjiang Institute of Ecology and Geography, CAS, 818 South Beijing Road, 830011 Urumqi, China. Tel.: +86 13079978645.
E-mail address: lulu_8401@yahoo.com (L. Lu).

0303-2434/$ – see front matter © 2010 Elsevier B.V. All rights reserved.
doi:10.1016/j.jag.2010.12.007

algorithms utilizing observations from two or even more channels have also shown improved quality of LST retrieval (Coll and Caselles, 1997; Sun and Pinker, 2003; Venus and Rugege, 2004; Yang and Yang, 2006).

Most of these studies focus on conditions without clouds, or filter cloud contaminated pixels to meet rigid algorithm assumptions. However, on a global scale, it has been demonstrated that global mean cloud cover and land-surface temperature are not independent (Paltridge, 1974; Groisman et al., 2000; Dai et al., 1999). On a regional scale, cloudy-sky conditions represent more than half of the actual day-to-day weather, and the presence of clouds modifies the surface energy budget significantly (Jin, 2000). Therefore, the interaction between clouds and surface temperature deserves more attention. Estimating LST under clouds is highly significant in remote sensing research. The spatially distributed LST data, including LST during cloudiness with a high temporal resolution, are important for several modeling applications (Venus and Rugege, 2004; Schneider et al., 1978). However, it is difficult to derive the LST of cloudy pixels directly from remotely sensed thermal infrared information, because under clouds LST cannot be measured due to absorption of the surface emission by the clouds. Microwave observations may be used to obtain LST under cloudy skies because of their ability to penetrate clouds. Some algorithms have been developed for retrieving LST based on passive microwave remotely sensed data, and achieved accuracies with an error of 3 K relative to the MODIS LST product (Mao et al., 2005; Jia et al., 2007) and RMSE varying between 1 and 6 K for the interpolated global LST diurnal cycle (Aires et al., 2004). However, most of these algorithms were specifically developed for clear sky conditions using simulated data, or were mainly implemented over bare soil. As the microwave signal is sensitive to the effects of surface roughness and vegetation, further study is needed to examine the applicability of these algorithms under cloudy conditions as well as in situations where the ground surface is covered by vegetation.

Jin (2000) proposed a 'neighboring-pixel' approach to estimate LST of cloudy pixels from polar-orbiting satellites on the basis of surface energy balance, in which the LST of a cloudy pixel is interpolated by clear sky LST observations surrounding the cloudy pixel. The drawback of this approach is inevitable because the surrounding pixels may not necessarily be representative, i.e. albedo, emissivity, and other driving variables may change significantly between pixels in heterogeneous areas. Instruments on board geo-stationary satellites, however, provide adequate samplings to capture the diurnal cycle of LST (Aires et al., 2004; Venus and Rugege, 2004). The geo-stationary satellite Meteosat Second Generation (MSG), developed by the European Space Agency (ESA) and EUMETSAT, has a main imager sensor called Spinning Enhanced Visible and Infrared Imager (SEVIRI), which provides measurements at temporal intervals of 15 min in 12 spectral channels. The importance of the temporal resolution of geo-stationary satellite data in obtaining LSTs and the necessity of retrieving LSTs under cloudy conditions lead to the formidable challenge of extending the application of the neighboring-pixel approach proposed by Jin (2000) to quarter hourly MSG/SEVIRI observations, and to fully capitalize on the temporal domain of the data offered by the geo-stationary satellite sensor.

The objective of this study is to estimate the LST under clouds from MSG/SEVIRI observations. The methodology is presented in Section 2, and materials including satellite measurements as well as ground-based measurements are described in Section 3. Results from the proposed method are addressed in Section 4, and compared with the measurements recorded at ground level. Discussion of uncertainties in the model and its input parameters, effects of the parameterization on estimates of cloudy sky LST, as well as error analysis are presented in Section 5. The paper closes with conclusions and recommendations in Section 6.

2. Methodology

2.1. Retrieval of LST under a cloudy sky

In this study, LST under a cloudy sky is retrieved based on the neighboring-pixel approach reported in Jin (2000). This approach is developed on the basis of the theory of surface energy balance, in which the relationship between energy fluxes is formulated as:

$$S_n - F_n = G + H + LE \tag{1}$$

where S_n is net solar (or shortwave) radiation, F_n is net longwave radiation, G is ground heat flux, and H and LE denotes sensible heat flux and latent heat flux, respectively. S_n derives from incoming shortwave radiation minus outgoing shortwave radiation. F_n is defined as up-welling longwave radiation minus down-welling longwave radiation. In Eq. (1), the up-welling longwave radiation is a direct function of surface temperature T_s as well as surface emissivity, and both H and LE are also functions of T_s, whereas T_s is the variable to be retrieved in this study. The other parameters necessary to obtain H and LE, including air density at surface layer, specific heat at constant pressure, wind speed, specific humidity at T_s and specific humidity at a reference level, can not be measured by satellites. Alternatively, with every term in Eq. (1) being partially differentiated with respect to T_s, there is

$$\frac{\partial G}{\partial T_s} = \frac{\partial S_n}{\partial T_s} - \frac{\partial F_n}{\partial T_s} - \frac{\partial S_{hle}}{\partial T_s} \tag{2}$$

where S_{hle} is the sum of H and LE. In Eq. (2), the mathematical expression $\partial S_n/\partial T_s$ does not mean net solar radiation is a function of T_s, but it is valid viewing from $S_n = G + F_n + S_{hle}$ in which S_n is equal to the T_s-related energy terms. On the basis of the force-restore method (Deardorff, 1978; Dickinson, 1988; Jin, 2000):

$$G = k_g \frac{\partial T}{\partial Z} = k_g \frac{T_s - T_d}{\Delta Z} \tag{3}$$

where k_g is thermal conductivity of ground soil in unit of $\mathrm{W\,m^{-1}\,K^{-1}}$; ΔZ is the penetration depth defined as a function of the thermal diffusivity which is the ratio of thermal conductivity to volumetric specific heat; and T_d is the temperature at a depth beyond the penetration of the periodic oscillation. Since the temperature T_d is much less sensitive to surface insolation than the surface temperature (Stull, 1988; Jin, 2000), there is

$$\frac{\partial G}{\partial T_s} = \frac{\partial}{\partial T_s}\left[k_g \frac{T_s - T_d}{\Delta Z}\right] \approx \frac{k_g}{\Delta Z} \tag{4}$$

The variables of H and LE cannot be derived from satellite observations, however, analysis of ground observations of several sites and simulated data using single-column CCM3 (Community Climate Model) in Jin (2000) shows linear relationships between F_n and S_n, as well as between S_{hle} and S_n:

$$F_n = a_0 + aS_n \tag{5}$$

$$S_{hle} = b_0 + bS_n \tag{6}$$

The coefficient a is a function of surface soil properties, and b is a function of local surface and soil properties.

Therefore, there are

$$\frac{\partial F_n}{\partial T_s} = \frac{\partial F_n}{\partial S_n}\frac{\partial S_n}{\partial T_s} = a \cdot \frac{\partial S_n}{\partial T_s} \tag{7}$$

and

$$\frac{\partial S_{hle}}{\partial T_s} = \frac{\partial S_{hle}}{\partial S_n}\frac{\partial S_n}{\partial T_s} = b \cdot \frac{\partial S_n}{\partial T_s} \tag{8}$$

Combining (4), (7), and (8) gives:

$$\frac{\partial S_n}{\partial T_s} = \frac{k_g}{\Delta Z}\frac{1}{1-a-b} \tag{9}$$

Then the "neighboring clear pixel" is defined as a clear pixel with similar vegetation, soil, and topographic conditions to the cloudy pixel. The term "neighboring" can be used in either a spatial or a temporal sense. Therefore, it can be assumed that the difference in net solar radiation as well as in surface temperature between two pixels or moments is only caused by clouds. The differential in Eq. (9) can be approximated to a finite difference with the meaning of difference of net solar radiation between two neighboring pixels and difference of surface temperature between the two neighboring pixels. As a result, Eq. (9) can be written as

$$\Delta T_s = \frac{1}{\lambda}(1-a-b)\,\Delta S_n = \frac{1}{K}\,\Delta S_n \tag{10}$$

where $\lambda = k_g/\Delta Z$, and $1/K = 1-a-b/\lambda$, ΔT_s is difference of T_s between two adjacent pixels (i.e. the pixel contaminated by clouds and its adjacent pixel under clear sky), ΔS_n is the difference of net solar radiation between the two adjacent pixels.

Consequently, T_s of a cloudy pixel is represented as:

$$T_{cloud}(i) = T_{clear}(j) + \frac{1}{K}\Delta S_n(i,j) \tag{11}$$

with T_{cloud} being T_s of the cloudy pixel i, T_{clear} being T_s of the temporally or spatially neighboring pixel j (i.e. a pixel without clouds), ΔS_n being the difference of net solar radiation between pixel i and j.

In this study, T_{cloud} is interpolated using Eq. (11) in the temporal sense, that means T_s of a pixel at an overcast occasion is interpolated by its T_s at the closest previous occasion without clouds. According to Eq. (11), T_{cloud} is related to solar radiation, hence estimation of T_{cloud} in nighttime is not referred to here.

2.2. Retrieval of LST under a clear sky

Highly accurate estimation on T_s of pixels without clouds from satellite infrared radiometers is essential, but forms a challenging task, either due to atmospheric attenuation and emission of thermal radiation, or to the nonblack-body property of the surface (Li and Becker, 1993). The classical split-window algorithm is the most popular tool, and forms the basis for the development of various improved methods to eliminate perturbations (Becker and Li, 1990, 1995; Sobrino et al., 1994; Coll and Caselles, 1997). Using multi-bands observations of SEVIRI, including mid-infrared and thermal infrared wavelengths, Sun and Pinker (2007) developed a 4-channel algorithm by adding another split-window, observations from channels of 3.9 μm and 8.7 μm, for further removal of atmospheric distortions. In Sun and Pinker (2007), the 4-channel algorithm was compared with two other algorithms, i.e. the split-window algorithm proposed by Sun and Pinker (2003) and the generalized split window algorithm developed by Wan and Dozier (1996) on the basis of the local split-window algorithm reported by Becker and Li (1990). It was demonstrated that the 4-channel algorithm gave the best retrievals (a maximum bias error of −1.5 K against −3 K produced by Wan and Dozier (1996) and −1.5 K in Sun and Pinker (2003)).

In the 4-channel algorithm, the formula to estimate T_s during nighttime is:

$$T_s(l) = a_0(l) + a_1(l)T_{10.8} + a_2(l)(T_{10.8}-T_{12}) + a_3(l)(T_{3.9}-T_{8.7}) + a_4(l)(T_{10.8}-T_{12})^2 + a_5(l)(\sec\theta - 1) \tag{12}$$

where T represents the brightness temperature, with the digital subscript representing the wavelength, θ is the satellite viewing angle, l is the surface type index, and a_i are the regression coefficients dependent on surface type.

For the daytime, a solar correction is introduced to reduce contamination by solar signal in the brightness temperature, resulting in T_s being represented as:

$$T_s(l) = a_0(l) + a_1(l)T_{10.8} + a_2(l)(T_{10.8}-T_{12}) + a_3(l)(T_{3.9}-T_{8.7}) + a_4(l)(T_{10.8}-T_{12})^2 + a_5(l)(\sec\theta - 1) + a_6(l)T_{3.9}\cos\theta_s \tag{13}$$

where θ_s is the solar zenith angle. The coefficients in Eqs. (12) and (13) are not identical as presented in Sun and Pinker (2007), and are determined from the forward simulations using the Moderate Resolution Atmospheric Radiance and Transmittance Model (MODTRAN 3.7) on 14 land cover types derived from UMD (Department of Geography, University of Maryland). Therefore, surface type information can be used in the 4-channel algorithm instead of surface emissivity. In the present study, a cloudy layer mask is used for cloud screening, in which the average value and the standard deviation of brightness temperature in the infrared channels at 8.7 μm, 9.7 μm, 10.8 μm, 12 μm and 13.4 μm are calculated. If the product of the average value and the standard deviation is less than the empirical threshold of 2884.7116, the pixel is determined as a cloudy pixel.

2.3. Retrieval of all-sky global radiation

The aim of the Heliosat-2 method, developed by the Télédétection and Modélisation group, Center d'Energétique, is to transfer images derived from the satellite Meteosat onto maps of solar radiation at ground level. As most methods for estimating solar radiation from satellite observations, this method assumes the difference of solar radiation derived from the satellite is only caused by changes in apparent albedo observed by the space-borne sensor. Therefore, in this study it is assumed that, apart from differences in solar angle and viewing angle, the difference in solar radiation between two neighboring pixels, or of the same pixel on two different occasions, is mainly due to the appearance of clouds.

For the Heliosat-2 method, the key parameter is cloud index, which can be dated back to Möser and Raschke (1984). It is usually denoted as n, and can be written as (Li et al., 1993; Beyer et al., 1996; Dagestad and Olseth, 2007):

$$n = \frac{\rho - \rho_{ground}}{\rho_{cloud} - \rho_{ground}} \tag{14}$$

where ρ is the reflectance (or apparent albedo) observed by the visible imager aboard the satellite, here the HRV (High Resolution Visible) channel of the SEVIRI sensor; ρ_{ground} is the ground reflectance under clear skies; and ρ_{cloud} is the reflectance of the brightest clouds. If the sky is clear, the apparent albedo ρ is close to the ground reflectance and the cloud index n is close to 0 (possibly negative). If it is overcast, the cloud index n is close to 1 (possibly larger). In this study, a modified method proposed by Dagestad and Olseth (2007) is used to calculate the cloud index, in which ρ_{ground} is parameterized into a 3rd order polynomial of the co-scattering angle delineating sun-ground-satellite geometries (Dagestad, 2004). As a result, the dependence of the reflectance on the viewing geometry is taken into account, and probable effects (i.e. non-lambertian reflection from the ground surface itself, varying amounts of shadow due to nearby terrain and broken clouds, scattering and absorption due to interaction with air molecules, aerosols and clouds) are corrected. According to Dagestad and Olseth (2007), the 4-percentile value of the reflectance within each 10° bin of the co-scattering angles is calculated to fit the 3rd order polynomial. To avoid outliers, the 98 percentiles of reflectance are set as ρ_{cloud} instead of the maximum value.

Table 1
Data source summary.

Parameter	Instrument	Resolution	Height	Accuracy	Date	Site
Land cover (UMD)	MODIS	1 km	–		–	–
Brightness temperature	MSG/SEVIRI	3 km	–	–	June, 2008	Kenya
			–	–	September, 2005	Burkina Faso
Broadband reflectance	MSG/SEVIRI	1 km	–	–	June, 2008	Kenya
			–	–	September, 2005	Burkina Faso
Surface temperature	Everest Infrared Thermometer	–	–	±0.5 °C	June 2008	Kenya
					September, 2005	Burkina Faso
Meteorolog-ical data	ADAS	–	0.5 m & 1.5 m	–	June, 2008	Kenya
	Meteorologi-cal station	–	2 m	–	September, 2005	Burkina Faso
Longwave radiation balance (up & downward)	CNR1 Pyranometer (Kipp&Zonen, NL)	–	2 m	±2.0%	September, 2005	Burkina Faso
Shortwave radiation balance (up & downward)	CNR1 Pyranometer (Kipp&Zonen, NL)	–	2 m	±2.0%	September, 2005	Burkina Faso

Table 2
Evaluation on retrieved T_{clear} and T_{cloud}.

	Kenya		Burkina Faso	
	Bias (K)	RMSE (K)	Bias (K)	RMSE (K)
T_{clear} from 4-channel algorithm	0.34	2.49	0.85	2.82
T_{cloud} from T_{clear}(g) and S_n(g)	2.71	4.11	−0.8	2.25
T_{cloud} from T_{clear}(s) and S_n(s)	−3.68	5.55	0.37	5.11
T_{cloud} from T_{clear}(s) and S_n(g)	−3.06	5.08	−1.4	4.83
T_{cloud} from T_{clear}(g) and S_n(s)	2.85	4.60	0.81	4.52

T_{cloud} stands for T_s under a cloudy sky; T_{clear} is T_s under a clear sky.

Using the empirical relationship between the clear sky index and the cloud index, solar radiation is calculated as follows:

$$k = \begin{cases} 1.2 & \text{for } n < -0.2 \\ 1 - n & \text{for } n \in [-0.2, 0.8] \\ 2.0667 - 3.6667n + 1.6667n^2 & \text{for } n \in [0.8, 1.1] \\ 0.05 & \text{for } n > 1.1 \end{cases} \quad (15)$$

with k being the clear sky index defined as:

$$k = \frac{R}{R_{clear}} \quad (16)$$

R is the actual solar radiation, and R_{clear} is the solar radiation under a clear sky which is obtained with the method proposed by Hammer et al. (2003). To achieve this, the Linke turbidity factor is calculated according to Molineaux and Ineichen (1996).

3. Data

3.1. Satellite data

The 12 spectral channels of MSG/SEVIRI cover a range of the visible, near infrared and thermal infrared spectrum. Of these 12 channels, 8 have wavelengths in infrared domain. Brightness temperature from the atmospheric water vapor absorption bands (6.2 μm and 7.3 μm), the ozone absorption band (9.7 μm) and the CO_2 absorption band (13.4 μm), as well as the remaining four atmospheric window bands (3.9, 8.7, 10.8 and 12.0 μm) are used to estimate LST here. The HRV channel provides information of the surface along a broad spectrum, ranging from 0.4 to 1.1 μm. In this study, reflectance derived from the HRV channel is used to estimate solar radiation. Additionally, to drive the model for estimating T_s under clear skies, the MODIS yearly 1 km land cover data are used as a surrogate for land surface emissivity (LSE) (Table 1). The MODIS product can identify 17 classes of land cover in the International Geosphere–Biosphere Programme (IGBP) global vegetation classification scheme, including the UMD 14 classes and additional three land cover types, i.e. permanent wetlands, cropland/natural vegetation mosaic, and permanent snow and ice. In the present study, the additional three land cover types are reclassified into the UMD classes.

Table 3
Comparison of solar radiation derived from MSG against *in situ* measurements.

	n	Bias (W m^{-2})	RMSE (W m^{-2})
Kenya	976	50.31	131.88
Burkina Faso	748	71.07	217.60

3.2. Data from field experiments

For parameterization and validation, *in situ* data collected during two experiments are used: (1) meteorological data of Naivasha, Kenya measured by an Automatic Data Acquisition System (ADAS) with the data logger HOBO H21-001; (2) meteorological data of Dano, Burkina Faso in west Africa with a latitude of 11°09′42.2″N and a longitude of 3°04′34.1″W. For the site in Burkina Faso, it is a tree savannah landscape, however with grass dominating in the proximity of the meteorological station. The ADAS in site of Kenya was located at a latitude of 0°16′40″S, and a longitude of 36°29′03″E, 40 km north of Lake Naivasha, a valley floor of the Aberdare Mountains. Grass dominated within a 5 km radius around the ADAS. Sensors measuring wind speed/wind direction, air temperature, and relative humidity were installed there at two heights, while incoming solar radiation was measured by pyranometer. In site of Burkina Faso, all sensors, including the pyranometers used to measure up- and downward longwave radiation as well as up- and downward shortwave radiation, were installed at 2 m above the surface (Table 1). Infrared, non-contact thermometers were used to measure the surface temperature. Data of June 2008 in Kenya and of September 2005 in Burkina Faso collected at 15 min intervals were used for calculation in this study.

For Kenya, net longwave radiation F_n could not be derived from the instrument due to the lack of a corresponding pyranometer. Instead, F_n is calculated using the following formula (Allen et al., 1998; Nandagiri and Kovoor, 2005):

$$F_n = \sigma T_{air}^4 (0.34 - 0.14\sqrt{e_a}) \left(1.35\frac{S_\downarrow}{S_0} - 0.35\right) \quad (17)$$

where σ is the Stephan–Boltzmann constant, i.e. $(4.903/(24 \times 4)) \times 10^{-9} = 5.107 \times 10^{-11}$ MJ K^{-4} m^{-2} (¼ h^{-1}); T_{air} is the air temperature; e_a is the actual vapor pressure; $S_\downarrow/S_{0\downarrow}$ is the relative shortwave radiation, $S_\downarrow$ is incoming solar radiation measured by the pyranometer, and $S_{0\downarrow}$ is the clear sky solar radiation. $S_{0\downarrow}$ is derived from FAO 56 method (Allen et al., 1998). S_{hle} is calculated by using the following equation:

$$S_{hle} = S_n - F_n - G \quad (18)$$

If we define R_n as the net radiation, then there is $R_n = S_n - F_n$. It has been demonstrated that the ground heat flux G correlates with R_n, and can be calculated if the value of R_n is known (Reginato et al., 1985; Zhang, 1996). Based on observations over many years, Zhang (1996) reported that G is 20–50 percent of R_n for bare soil

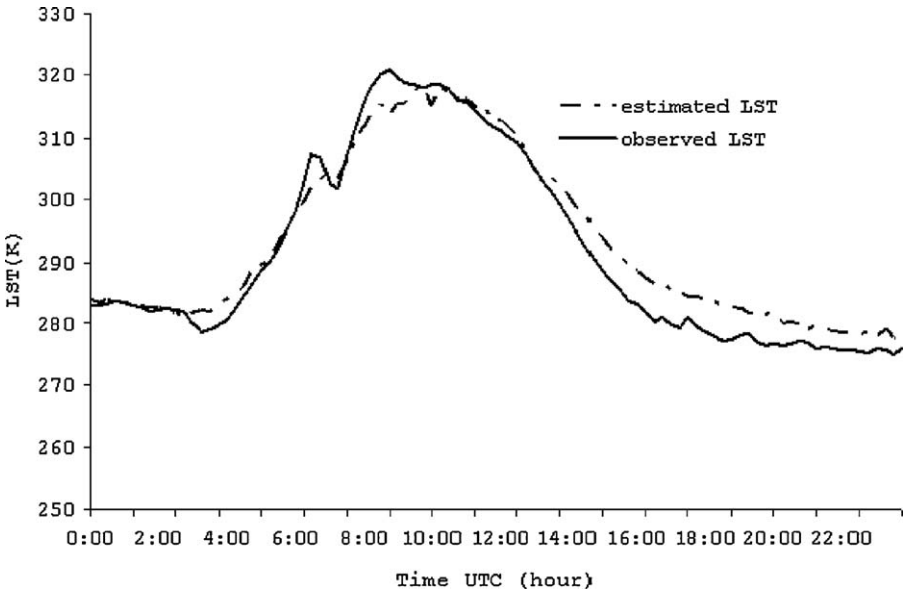

Fig. 1. *In situ* measured surface temperature (observed LST) and surface temperature estimated using the 4-channel method (estimated LST) for the site in Kenya (13/6/2008).

conditions, and 5–20 percent of R_n for vegetated surface. Allen et al. (1998) also proposed that G can be approximated to $0.1R_n$ for hourly or shorter periods during daytime. Therefore, in the present study, the assumption is made as $G = 0.1R_n$. S_{hle} in Burkina Faso is also calculated using Eq. (18), while the net longwave radiation is from measurements of the CNR1 2xCG3 Pyranometer (5–50 μm). All data used in this study are summarized in Table 1.

4. Results

4.1. LST under a clear sky

T_{clear} in Eq. (11) is retrieved by applying the 4-channel algorithm to observations of SEVIRI as shown in Fig. 1. Comparing against the *in situ* measured surface temperature, validation on retrieved T_{clear} reveals a bias error of 0.34 K for site in Kenya, and of 0.85 K for site in Burkina Faso (Table 2), where the bias error is derived from the estimated data minus the *in situ* data. The bias errors produced by the 4-channel algorithm concur with the results obtained by Sun and Pinker (2007) as described earlier. The RMSE (Root Mean Square Error) for site in Kenya is 2.49 K, and 2.82 K for site in Burkina Faso (Table 2).

For the 4-channel algorithm, coefficients a_i in Eqs. (12) and (13) are determined by surface type index. Therefore, misclassifying surface type may cause errors in the estimation of surface temperature. A series of SEVIRI brightness temperatures over the surface type of grass were simulated by using MODTRAN 4.0 in which the tropical atmosphere was assumed. Based on these simulated SEVIRI observations, an analysis on the sensitivity of 4-channel algorithm to the choice of land use class is performed (Fig. 2). In Fig. 2, RMSEs of LST estimated by 4-channel algorithm with choice of different land use classes are presented, including difference between RMSEs of estimated LST with a choice on other classes and the estimated LST error under the choice of grassland (i.e. difference of errors). It reveals that errors of LST derived from the 4-channel algorithm increase by less than 0.5–5 K if the wrong land use class is chosen.

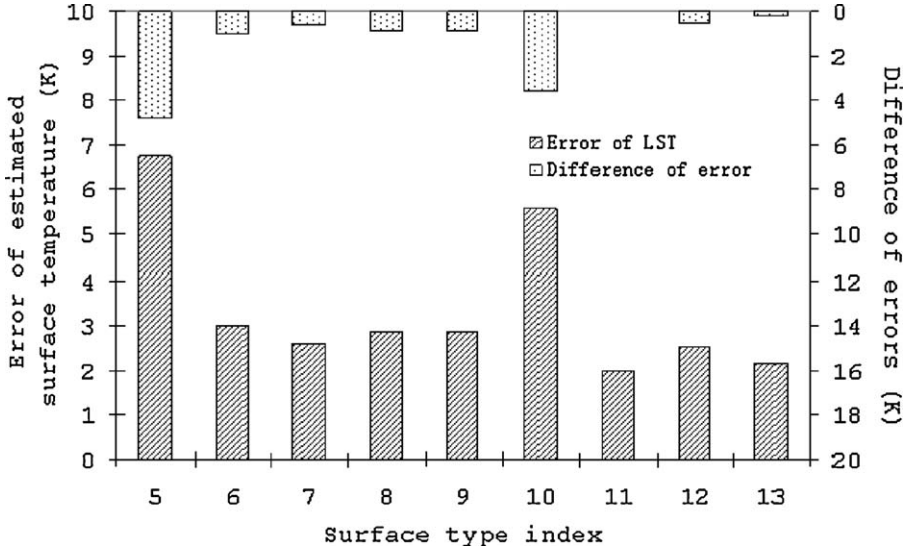

Fig. 2. Sensitivity of the 4-channel algorithm to surface type index (5-deciduous broadleaf forest, 6-mixed forest, 7-woodland, 8-wooded grassland, 9-closed shrub land, 10-open shrub land, 11-grassland, 12-cropland, 13-bare ground).

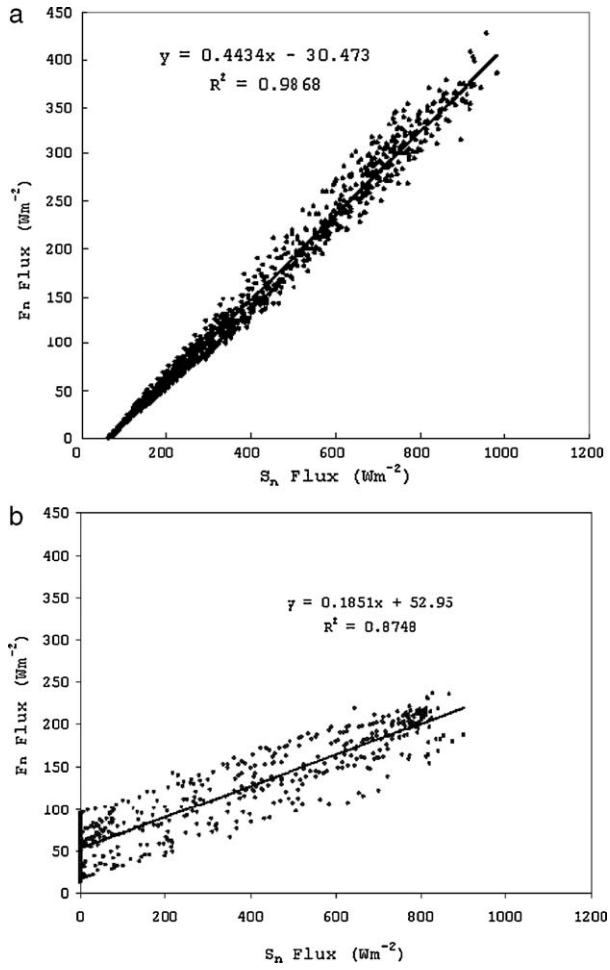

Fig. 3. Correlation between net solar radiation (S_n) and net longwave radiation (F_n) over (a) site in Kenya, and (b) site in Burkina Faso.

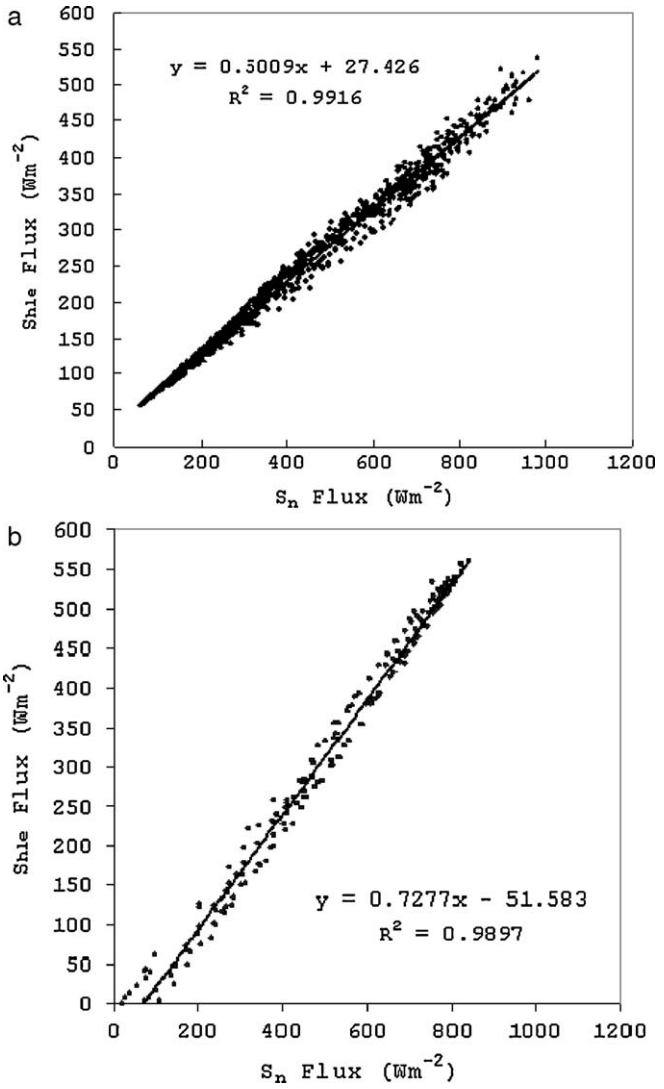

Fig. 4. Correlation between net solar radiation (S_n) and the sum of sensible and latent fluxes (S_{hle}) over (a) site in Kenya, and (b) site in Burkina Faso.

Both sites in Kenya and in Burkina Faso are savannas which are classified into grassland in IGBP and in UMD classification. In the proximity of the weather stations installed in the two sites, grass dominates, and a typical grass surface emissivity of 0.95 (Brutsaert, 1982; Katul et al., 1998) is used to convert radiometric values to surface temperatures. Therefore, the error due to mischoice of land use type is excluded from the uncertainty in LST derived from the 4-channel algorithm in this study.

4.2. All-sky global radiation

The Heliosat-2 method is applied to the SEVIRI observations in June 2008 of the site in Kenya, and in September 2005 of the site in Burkina Faso. A validation on the estimated solar radiation is performed against the *in situ* measurements (Table 3). In a review of researches on retrieval of solar radiation from satellite observations, bias errors derived from different algorithms are seen to range from 10 W m^{-2} to more than 100 W m^{-2} (Şenkal and Kuleli, 2009; Perez et al., 2002; Pinker et al., 1995). Thus, the bias errors of estimated solar radiation shown in Table 3 are comparable with those in other researches.

4.3. LST under a cloudy sky

4.3.1. Determination of parameter K

Parameterizations of F_n and S_{hle} in both sites are plotted in Figs. 3 and 4. It shows that coefficient a in Eq. (10) is 0.4434 for Kenya, and 0.1851 for Burkina Faso. Coefficient b in Eq. (10) is 0.5009 for Kenya, and 0.7277 for Burkina Faso. Note that values of the coeffiecient a differ a lot between the two sites, though the land cover of both sites are dominated by grass. One of the reasons is that a as well as a_0 is related to the surface properties and may vary with locations. Jin (2000) presented a general range of the coefficient a as smaller than 0.2, and it could vary from 0.06 for forests to 0.15 for desert areas. For the site in Kenya, it implies that 44.34% of net solar radiation is balanced by net longwave radiation. From the other aspect, a validation on the FAO 56 method for calculating F_n (i.e. Eq. (17)) is performed on Burkina Faso. It produces a R^2 of 0.5666 between F_n derived from pyranometer measurements and from FAO 56, and the RMSE is 59.31 W m^{-2} with a bias error of 32.12 W m^{-2}. As a result, coefficient a is 0.2763, and b is 0.6237. Comparing with a fitted by F_n and S_n derived from pyranometer measurements (a = 0.1815), application of the FAO 56 method introduces an overestimation of a. In spite of this, the results from Eq. (17) are used as the best guess of net longwave radiation when the actual measurements are not available in Kenya.

For both study sites, figures for ΔZ are not available, however, Dickinson (1988) reported $\Delta Z \approx 0.1$ m within a factor of 2 for a wide range of snow and soil conditions and for diurnal periodicity. The value of ΔZ is assumed to be 0.1 m. In the site of Kenya, the soil type is known as clay. Peters-Lidard et al. (1998)

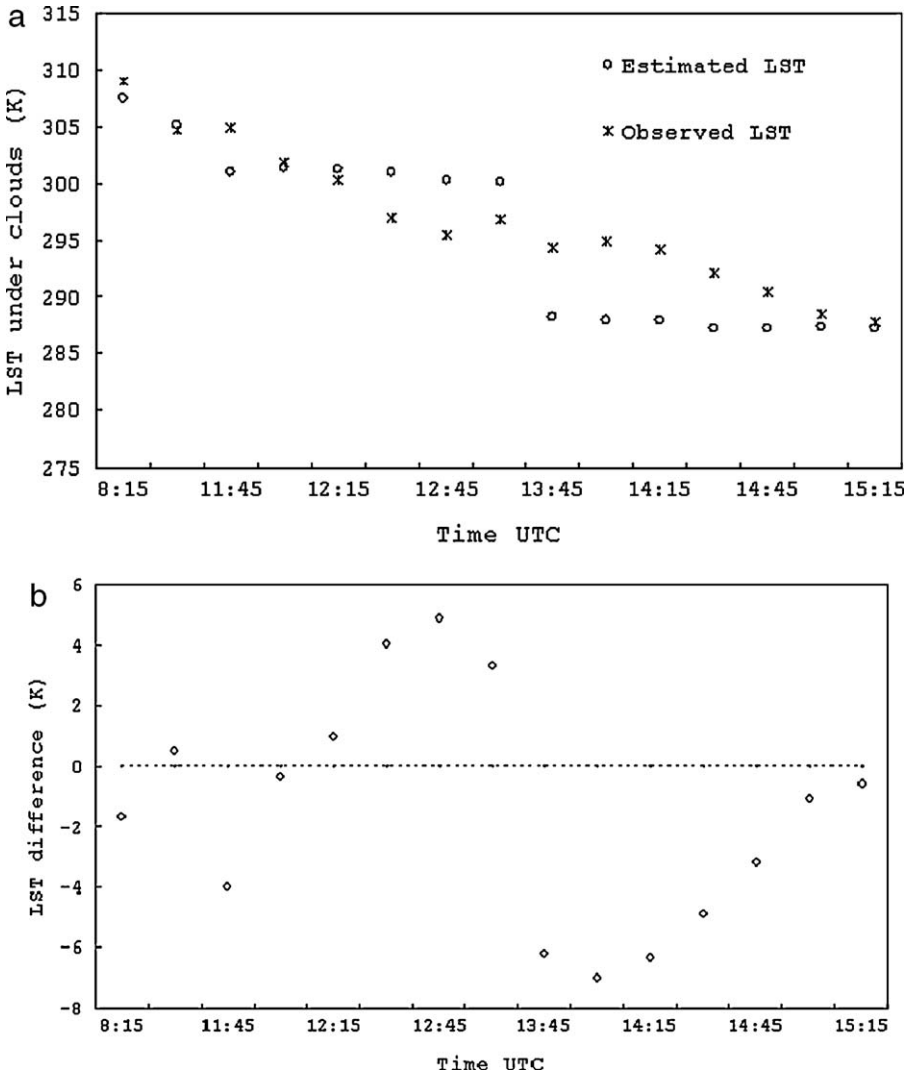

Fig. 5. (a) Comparison of LST under clouds estimated from satellite acquisitions (estimated LST) and *in situ* measurements (observed LST); (b) LST difference between estimated data and *in situ* data over site in Kenya (4/6/2008).

reported values of soil thermal conductivity of clay with porosity of 0.4 and quartz content of 0.25 at different level of saturation, from which we arbitrarily choose the value of 1.17 $W\,m^{-1}\,K^{-1}$ at mid-level saturation as the soil thermal conductivity in Kenya. For the site in Burkina Faso with latitude of 11°09′42.2″N and longitude of 3°04′34.1″W, Brümmer et al. (2008) described the soil types of its three adjacent sites as loam, including site 1 at 11°09′52.9″N, 3°05′03″W, site 2 at 11°09′53.2″N, 3°05′01.4″W, and site 3 at 11°09′53.6″N, 3°05′02.7″W. Correspondingly, the bulk density of the soil in the three sites is $1.58 \pm 0.02\,g\,cm^{-3}$, $1.47 \pm 0.03\,g\,cm^{-3}$, and $1.59 \pm 0.04\,g\,cm^{-3}$, respectively. According to Abu-Hamden and Reeder (2000), soil thermal conductivity of loam varies between 0.29 and 0.76 $W\,m^{-1}\,K^{-1}$ when the soil density is between 1.23 and 1.59 $g\,cm^{-3}$ with water content ranging from 1.4 to 21.2%. This is also consistent with soil thermal conductivity ranging from 0.15 to 0.79 $W\,m^{-1}\,K^{-1}$ proposed in Ghuman and Lal (1985). Combining knowledge discussed previously, the soil thermal conductivity is determined to be 0.79 $W\,m^{-1}\,K^{-1}$ for Burkina Faso. Therefore, the value of K in Eq. (10) is 210.05 $W\,m^{-2}\,K^{-1}$ for Kenya, and 90.6 $W\,m^{-2}\,K^{-1}$ for Burkina Faso.

4.3.2. Estimation of LST under a cloudy sky T_{cloud}

In this study, T_s under clear sky and net solar radiation derived from satellite observations are denoted as $T_{clear}(s)$ and $S_n(s)$, respectively. Likewise, T_s under clear sky and net solar radiation from ground-based measurements are denoted as $T_{clear}(g)$ and $S_n(g)$. Viewing individual day, taking June 4, 2008 for site in Kenya as an example, the dynamics of T_{cloud} in Eq. (11), that is estimated by the proposed algorithm using $T_{clear}(s)$ and $S_n(s)$, agrees with the ground-based measurements as shown in Fig. 5(a). The temperature difference between estimated T_{cloud} and ground-based measurements is generally up to 4 K (Fig. 5(b)). However, there are also occasions with extreme large differences of up to 7 K.

A validation on the algorithm is performed against the ground-based data for both sites, and the accuracy of T_{cloud} from $T_{clear}(s)$ and $S_n(s)$ in Table 2 shows a RMSE of 5.55 K for site in Kenya and 5.11 K for site in Burkina Faso. The result is also plotted in Fig. 6, and points interpolated at only one time step of 15 min and the ones interpolated at further time steps are marked. Contrasting to scattered points interpolated at more than one time step of 15 min, the points interpolated at only one time step of 15 min seems to be more convergent to the 1:1 line in Fig. 6(b), except the outlier at the estimated value of 293.94 K. It indicates that the quality of the interpolation decreases when the distance to the last real observation of LST under a clear sky increases. In Fig. 6(a), some of the points are outlying around 285 K because of underestimation of their last real values of remote sensing LST. Analyzing on the LST estimated by 4-channel algorithm shows a bias of −5.16 K of the

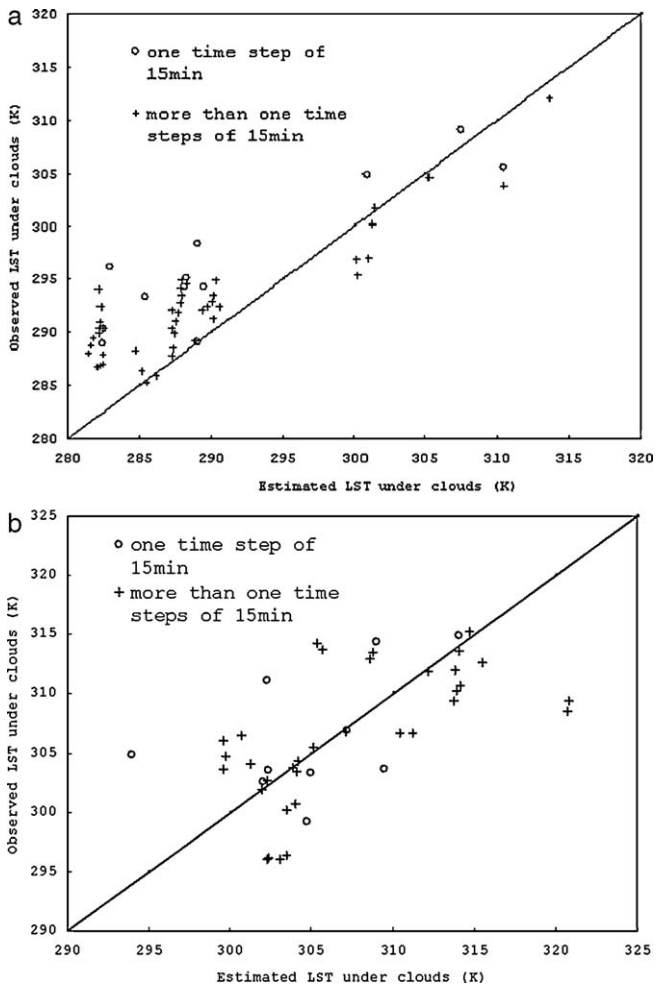

Fig. 6. Comparison of LST under clouds estimated by the algorithm with *in situ* data in (a) Kenya, and (b) Burkina Faso (the line is the 1:1 line).

last real values of remote sensing LST, which consequently causes underestimation of LSTs during a time series overcast. A similar situation is also presented in Fig. 5(a). It reveals that T_{clear} at the occasion next the time when overcast weather starts tends to be underestimated, especially for occasions when the adjacent pixels are overcast or between two time series when cloudiness appears consecutively.

4.3.3. Spatial interpolation versus temporal interpolation

To compare the proposed method with spatial neighboring-pixel approach, the spatial neighboring-pixel approach is also performed on the site in Kenya, in which the 'neighboring clear pixel' is spatially adjacent to the cloudy pixel under analysis. Fig. 7 shows that the median of difference between ground-based measurements and estimated T_{cloud} from the temporal neighboring-pixel approach is smaller than the one produced by the spatial neighboring-pixel approach. This illustrates that the temporal neighboring-pixel approach has a higher accuracy in determining LST under cloud cover.

Additionally, surface temperatures in overcast conditions in Kenya are calculated with the temporal lag between the current overcast condition and the previous cloudless occasion being set as 1 day. Plotting the algorithm-produced T_{cloud} against the ground-based measurements (Fig. 8) shows a bias of −0.52 K. However, the RMSE of estimated T_{cloud} with the larger temporal lag is much higher (9.21 K versus 5.55 K in Fig. 6(a)). This indicates that the temporal autocorrelation of LST decreases with an increase in temporal lag. Compared with polar-orbiting satellites, which overpass a given area usually only twice a day, geo-stationary satellites provide much more samples of the earth's brightness temperature, especially for the MSG satellite which has a temporal resolution as high as 15 min. Therefore, to estimate LST in overcast conditions and to reconstruct the LST diurnal cycle, observations from the geo-stationary satellite MSG give better results.

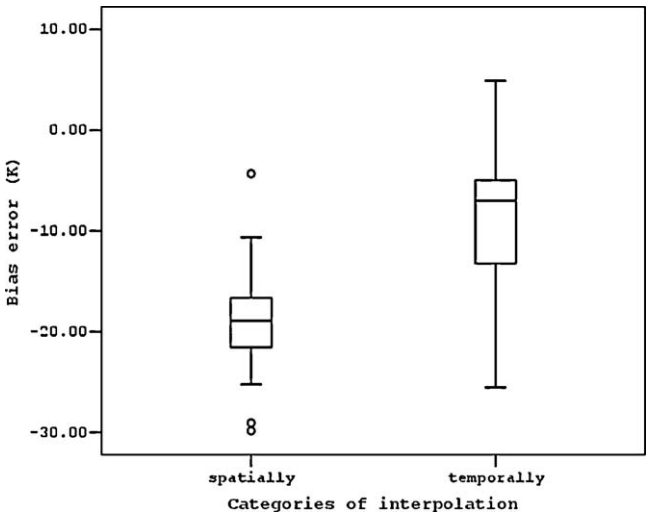

Fig. 7. Comparison of the error in satellite-based LST under clouds derived from the spatial neighboring-pixel approach with the error resulting from the temporal neighboring-pixel approach (site in Kenya).

5. Discussions

5.1. Error analysis

To examine the reliability of the temporal neighboring-pixel approach, T_{cloud} is estimated using the ground-based measurements $T_{clear}(g)$ and $S_n(g)$. This results in a RMSE of 4.11 K in Kenya, and of 2.25 K in Burkina Faso (T_{cloud} from $T_{clear}(g)$ and $S_n(g)$ in Table 2). Compared with errors of T_{cloud} produced by satellite-based estimations (T_{cloud} from $T_{clear}(s)$ and $T_{clear}(s)$ $S_n(s)$ in Table 2), the ground-based data analysis removes uncertainties of the 4-channel algorithm and the Heliosat-2 algorithm, and reveals only the uncertainty of the temporal neighboring-pixel scheme itself.

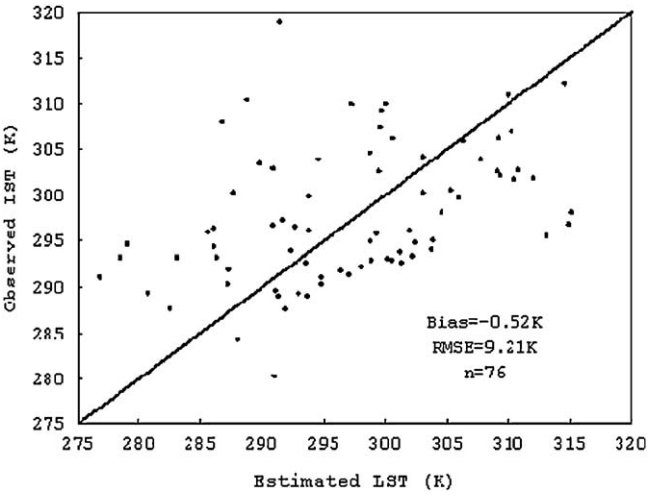

Fig. 8. Estimated LST under clouds with a large temporal lag (1 day) versus *in situ* data in Kenya (the line is the 1:1 line).

The ground-based net solar radiation S_n(s) and the satellite-based LST under a clear sky T_{clear}(s) are used to estimate T_{cloud}, and a RMSE of 5.08 K is obtained for site in Kenya and of 4.83 K for site in Burkina Faso. With reference to the errors in T_{cloud} from T_{clear}(s) and S_n(s), errors of T_{clear}(s) are fully translated into errors in estimation of T_{cloud}. Comparing T_{cloud} from T_{clear}(g) and S_n(s) with T_{cloud} from T_{clear}(g) and S_n(g), it shows that uncertainty of net solar radiation has different influences on error of estimated T_{cloud} between sites in Kenya and Burkina Faso. For the site in Kenya, incoming solar radiation $S_\downarrow$ measured by pyranometer presents an average of 193.89 W m^{-2} with standard deviation of 302.08 W m^{-2}, and RMSE of the estimated $S_\downarrow$ is 131.88 W m^{-2} as shown in Table 3. Due to K value of 210.05 W m^{-2} K^{-1} being equivalent to real values of $S_\downarrow$ and greater than error of estimated $S_\downarrow$, it weakens influence of uncertainty in estimated net solar radiation on errors of estimated T_{cloud}. For the site in Burkina Faso, the average value as 416.76 W m^{-2} and standard deviation of 352.76 W m^{-2} is obtained for real $S_\downarrow$. As shown in Table 3, the RMSE of estimated $S_\downarrow$ is as large as 217.6 W m^{-2} for Burkina Faso. Contrasting to statistics of $S_\downarrow$ from pyranometer and error of estimated $S_\downarrow$, a relative small value of 90.6 W m^{-2} K^{-1} for K leads to impact of error in net solar radiation being equivalent to contribution of uncertainty of T_{clear} to error of estimated T_{cloud}. Therefore, the biases are different between Kenya and Burkina Faso. With further analysis, the different biases between the two sites are due to their different locations and seasons, i.e. June in Kenya with latitude of 0°16′40″S, and September in Burkina Faso with latitude of 11°09′42.2″N, which causes difference in $S_\downarrow$. This also demonstrates that the accuracy of the neighboring-pixel approach varies per case, as reported by Jin (2000) that it produced a RMSE ranging from 1.23 K to 3.21 K when the neighboring-pixel approach was applied to FIFE data of July, BOREAS data of January and CCM3/BATS (Community Climate Model/Biosphere–Atmosphere Transfer Scheme) data of July.

For the term ΔS_n in Eq. (11), S_n derives from $S_\downarrow(1-\alpha)$, where α is the surface albedo, and $S_\downarrow$ is estimated by using the Heliosat-2 method. Therefore, small errors in individual values of S_n or $S_\downarrow$ may be amplified in ΔS_n. Considering Eq. (11), RMSE of estimating $S_\downarrow$ is significant as listed in Table 3, however, its influence on the retrieval of T_{cloud} differs from per case as discussion in the previous paragraph, in which value of K plays an important role. In Eq. (11), the parameter K is assumed to be constant. It reflects the influences of vegetation type, soil type, and soil moisture on surface temperature. The physical meaning of K is the ratio of solar radiation change and surface temperature change. Fig. 9 plots dependence of the uncertainty in estimated T_{cloud} on parameter K for both sites, in which T_{cloud} is calculated using ground-based observations T_{cloud}(g) and S_n(g). It illustrates that the accuracy of the neighboring-pixel approach is sensitive to a small value of K but varies only slightly for large values, especially for site in Kenya. In Jin (2000), uncertainties in the neighboring-pixel approach is attributed to effects of parameter K and the parameterization of component energy fluxes, and the error contributed by K is 2.6 K at the most. In Fig. 9, for the site in Kenya, the maximal RMSE of estimated T_{cloud} is 4.3 K within a scope of large K. Therefore, an appropriate K can reduce the errors in estimation of T_{cloud}. For example, the RMSE of estimated T_{cloud} is at a minimum when the value of K is 120 W m^{-2} K^{-1} in Kenya and 50 W m^{-2} K^{-1} in Burkina Faso.

5.2. Effect of parameterization

For the neighboring-pixel approach, the terms of net longwave radiation F_n, sensible heat flux H and latent heat flux LE are parameterized into net solar radiation S_n by using statistical relationships. This contributes to a RMSE of 1.50–1.96 K in estimation of T_{cloud} as reported in Jin (2000). Instead of parameterization, F_n and S_{hle} deriving from pyranometer measurements are applied to estimating T_{cloud}, in which S_{hle} is calculated using Eq. (18) on the basis of S_n and F_n from pyranometer measurements. A RMSE value of 2.9 K in estimates of T_{cloud} for site in Kenya, and 1.89 K for site in Burkina Faso are obtained. Comparing with the errors produced by the ground-based analysis shown in Table 2 (a RMSE of 4.11 K for Kenya and 2.25 K for Burkina Faso in T_{cloud} from T_{clear}(g) and S_n(g)), it reveals that the parameterization causes errors in estimating T_{cloud}. However, this is inevitable because it is a challenge to estimate the fluxes directly from satellite observations.

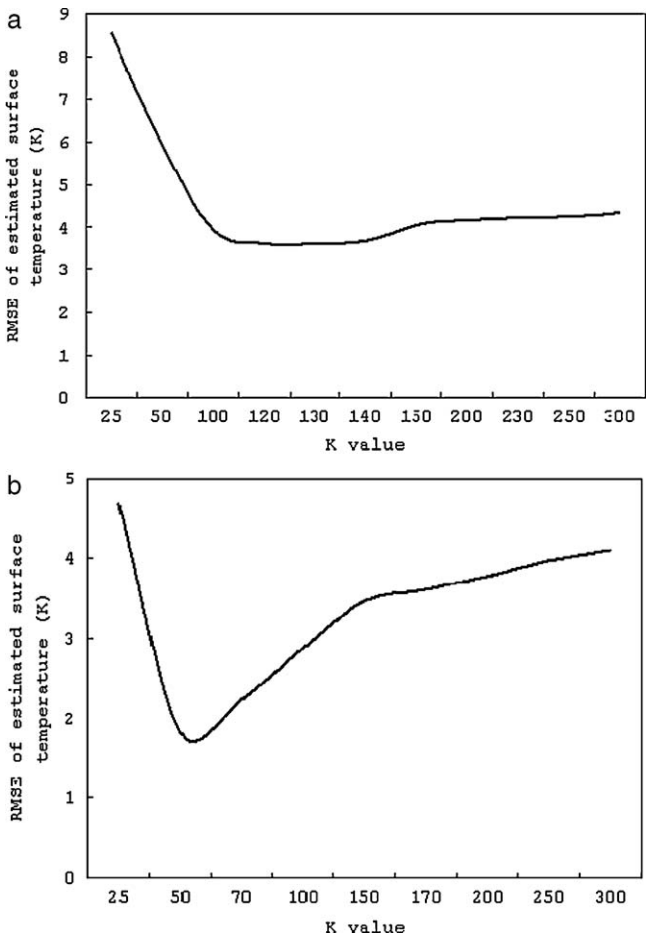

Fig. 9. Sensitivity of LST under clouds to coefficient K for (a) site in Kenya, (b) site in Burkina Faso.

5.3. Discussion on the model input parameters

As description in Section 3.2, S_{hle} is determined by Eq. (18). In that case, the derivative of S_{hle} to T_s in Eq. (2) could be rewritten as the derivative of R_n–G to T_s. The ground heat flux G is taken as a fixed fraction of R_n, denoted by γ, therefore, Eq. (11) can be written in an alternative form:

$$T_{cloud}(i) = T_{clear}(j) + \frac{\Delta Z}{k_g} \cdot \gamma \cdot (1-a) \cdot \Delta S_n(i,j) \quad (19)$$

It has been reported that ground heat flux G is neither constant nor negligible on diurnal timescales (Santanello and Friedl, 2003), and analysis on field observations shows that γ can range from 0.05 to 0.5 depending on the time of day, soil moisture and thermal properties, and vegetation amount and height (Kustas et al., 1993). As a result, setting fixed value to γ may directly introduce uncertainty to T_{cloud} in Eq. (19). Additionally, for input parameters of the model expressed as Eq. (19) or (11), ΔZ and k_g are interrelated, because the thermal diffusivity which is determined by k_g and vol-

Table 4
The absolute error values of the model parameters for seven scenarios.

Absolute error	Case						
	1	2	3	4	5	6	7
ΔT_{clear} [K]	1	2	4	1	1	2	4
Δa	0.01	0.05	0.1	0.01	0.01	0.01	0.01
Δb	0.01	0.05	0.1	0.01	0.01	0.01	0.01
$\Delta\gamma^*$	0.05	0.1	0.3	0.1	0.3	–	–
Δk_g [W m^{-1} K^{-1}]	0.05	0.1	0.5	0.05	0.05	0.05	0.05
$\Delta(\Delta Z)$ [m]	0.01	0.1	0.2	0.01	0.01	0.01	0.01
$\Delta S_{\downarrow}$ [W m^{-2}]	10	20	40	20 (*10)	40 (*10)	10	10
$\Delta\alpha$	0.01	0.05	0.1	0.01	0.01	0.01	0.01

Values of $\Delta S_{\downarrow}$ with the asterisk in cases 4 and 5 are used for evaluation in Eq. (19).

umetric specific heat appears in definition of the penetration depth ΔZ. Therefore, assuming ΔZ as 0.1 m and citing the values of k_g from the literatures would contribute errors to estimates of T_{cloud}. Including T_{clear} and ΔS_n in the right hand of Eq. (19) or (11), how errors of these input parameters propagate throughout the procedure, and consequently how the uncertainty and magnitude of estimated T_{cloud} depends on error propagation are important issues. To address these issues, an error propagation model is developed with the assumption that all the input parameters in Eq. (19) or (11) are independent. With this model, error propagation is evaluated to estimate impact of the absolute errors of the input parameters on estimates of T_{cloud}.

Given a function as:

$$Y = f(X) \tag{20}$$

sensitivity of the dependent variable Y to variable X in $f(X)$ is commonly defined by:

$$\Delta Y = \frac{\partial f}{\partial X} \cdot \Delta X \tag{21}$$

Table 4 shows the assumed absolute errors of input parameters for 7 cases: the best (1), the medium (2), and the worst case scenario (3) as well as the best case scenario with varying errors of downward shortwave radiation $S_{\downarrow}$ (case 4, taking $\Delta S_{\downarrow} = 20$; and case 5, taking $\Delta S_{\downarrow} = 40$) and the best case scenario with varying errors of T_{clear} (cases 6 and 7), for the model described as Eq. (11). It also shows the assumed absolute errors of the model parameters in Eq. (19) for 5 cases: the best (1), the medium (2) and the worst case scenario (3), and the best case scenario with varying errors of γ (cases 4 and 5, taking $\Delta S_{\downarrow} = 10$).

To illustrate the error propagation of the temporal neighboring-pixel approach, both sites are selected, and the absolute errors of estimated T_{cloud} under the 7 cases for Eqs. (11) and (5) cases for Eq. (19) are quantitatively listed in Tables 5 and 6, respectively.

In Table 5, taking site in Burkina Faso as an example, the average and standard deviation of the absolute error of T_{cloud} produced by Eq. (11) is 1.018 K and 0.01 K in the best case. One can observe increase of the average absolute error in cases 1, 4 and 5 in which absolute error of $S_{\downarrow}$ increases from 10 to 40 W m^{-2}, respectively, whereas the standard deviation varies between 0.009 and 0.01. On the other hand, the net solar radiation S_n is determined by $S_{\downarrow}(1-\alpha)$, where α is the surface albedo. For Burkina Faso, α is determined as 0.16 by the ratio of $S_{\uparrow}$ to $S_{\downarrow}$ measured with pyranometer. Due to the unknown value of α for the site in Kenya, we tentatively set it to the reference value for grass ($\alpha \approx 0.23$) as FAO 56. In reality, however, values of albedo may vary from time to time, and it also varies greatly at small spatial scales. Taking site in Burkina Faso as an example, setting a fixed value of 0.16 as the albedo results in a bias of −0.018 and a RMSE of 0.029 against the albedo derived from measured solar radiations. Therefore, uncertainty in determination of α would introduce errors in estimated T_{cloud}. The error propagation analysis shows an absolute error of 0.05 and 0.1 in albedo leads to the average absolute error of 1.059 K and 1.166 K with standard deviation of 0.056 K and 0.185 K, respectively, in estimation of T_{cloud} for the best case.

Table 5
The implemented Eq. (11), average and standard deviation of error in estimated T_{cloud}.

Site	Case	Absolute error	
		Average [K]	Stdev. [K]
Burkina Faso	1	1.018	0.01
	2	2.192	0.179
	3	4.398	0.374
	4	1.043	0.01
	5	1.138	0.009
	6	2.009	0.005
	7	4.005	0.003
Kenya	1	1.005	0.017
	2	2.061	0.221
	3	4.123	0.447
	4	1.009	0.017
	5	1.025	0.017
	6	2.003	0.009
	7	4.001	0.005

Comparison on cases 6 and 7 in Table 5 indicates that the average absolute error of T_{cloud} is sensitive to errors in T_{clear}. Therefore, for the medium and worst cases, the major contribution to uncertainty of T_{cloud} derives from errors of T_{clear}. Errors in other input parameters (i.e. a, b, k_g and ΔZ) only contribute small proportion to the average absolute error of T_{cloud} in cases 2 and 3, however, they cause obvious increase in the standard deviation comparing with other cases. In Eq. (11), the term of $(1-a-b)$ determines the parameter K, and the value of K is close to zero if we see the values of a and b of both sites. As a result, small relative errors in a and b may have major impact on the relative error of $(1-a-b)$, and consequently K may be very ill-defined. Applied F_n calculated with FAO 56 method to estimation of T_{cloud} with T_{clear}(s) and S_n(s), a

Table 6
The implemented Eq. (19), average and standard deviation of error in estimated T_{cloud}.

Site	Case	Absolute error	
		Average [K]	Stdev. [K]
Burkina Faso	1	1.053	0.051
	2	2.195	0.187
	3	4.58	0.577
	4	1.162	0.168
	5	1.878	0.833
Kenya	1	1.014	0.052
	2	2.049	0.18
	3	4.147	0.527
	4	1.043	0.153
	5	1.234	0.665

value of 79 W m^{-2} K^{-1} is obtained for K with $a = 0.2763$, $b = 0.6237$, and a RMSE of 5.47 K in estimated T_{cloud} is reported. Comparing with the RMSE 5.11 K of T_{cloud} from T_{clear}(s) and S_n(s) for Burkina Faso in Table 2, ill-defined K by a and b due to the uncertainty of F_n (RMSE = 59.31 W m^{-2}) causes an increase of 0.36 K for RMSE of estimated T_{cloud}. This also demonstrates that the error of F_n estimated with FAO 56 method is acceptable in this study. The error propagation shows that the average absolute error of T_{cloud} is 1.129 and 1.392 K with $\Delta a = 0.05$, $\Delta b = 0.05$, and $\Delta a = 0.1$, $\Delta b = 0.1$, respectively, when the absolute errors of other input parameters are set to the same values with the best case 1. Correspondingly, the standard deviation is 0.133 and 0.396 K.

For the model described as Eq. (19), results are in the same order of magnitude as those from Eq. (11). Comparison on the best, medium and worst cases of both sites as shown in Table 6 reveals that absolute error of T_{clear} contributes a large proportion to the average absolute error of estimated T_{cloud}. As it has been reported that γ can range from 0.05 to 0.5 (Kustas et al., 1993), the best case scenario (cases 1, 4 and 5) with absolute errors of γ varying from 0.05 to 0.3 is developed. Table 6 shows that the average absolute error of T_{cloud} is 1.053, 1.162 and 1.878 K for site in Burkina Faso, and 1.014, 1.043, and 1.234 K for site in Kenya, when error of γ is 0.05, 0.1, and 0.3. When the absolute error of γ increases, the standard deviation of the absolute error of T_{cloud} increases as well. Summarizing results in Tables 5 and 6, it seems that the error propagation of the temporal neighboring-pixel approach evaluated for both sites is in the same order of magnitude.

6. Conclusions and recommendations

The observations from MSG/SEVIRI may be used to estimate surface temperature at a high frequency to represent the diurnal cycle due to its temporal resolution being as high as 15 min. To achieve this goal, estimation of LST for cloudy pixels is required. A hybrid technique of the spatial "neighboring-pixel" approach and the "surface air temperature" approach has been developed to treat the cloudy pixels by Jin (2000), and has been implemented on polar-orbiting satellite observations. Aiming to complement the gap in application of this algorithm on geo-stationary satellite observations, the present study estimates LST of pixels contaminated by clouds by combining the 4-channel algorithm and the Heliosat-2 algorithm, in which the temporal neighboring-pixel approach is developed. As a result, an accuracy of around 5 K in estimates of LST under cloudy sky at quarter hourly, pixel level is achieved. An operational procedure and experiment for obtaining LST under cloud cover from MSG/SEVIRI data has also been outlined. Error propagation analysis on the proposed temporal neighboring-pixel approach reveals that the absolute error of estimates of LST under cloudy sky is less than 1.5 K in the best case scenario, and increases linearly with increase in the absolute error of LST under clear sky. Despite this uncertainty, the proposed method is able to retrieving the LST under a cloudy sky condition with acceptable accuracy for less demanding applications (e.g. biodiversity habitat suitability studies), and it provides the ability to reconstruct diurnal LST cycles from geo-stationary satellite observations particularly useful for regions where ground meteorological observations are scarce.

For the neighboring-pixel approach, it is assumed that the variation of LST is caused by variations in insolation (which in turn is related to cloudiness) during the daytime. At nighttime, clouds also affect the surface temperature, but then the longwave radiation from clouds rather than the variation in insolation impacts LST. Therefore, the neighboring-pixel approach can only be used during daytime. To reconstruct diurnal cycle of LST, a new appropriate method for estimating LST under cloudy sky during nighttime will be developed in the future. As error analysis indicates that errors of LST under clear sky from the 4-channel algorithm introduces major uncertainty to estimates of LST under cloudy sky, future studies could address the uncertainty in the clear-sky LST retrieval. Error propagation analysis revealed that uncertainties in the estimation of apparent albedo (0.05–0.1) lead to relatively large error in estimation of T_{cloud}. Additionally, improved parameterization of the ground heat flux is needed given the varying soil and rainfall properties, and strategy is needed to overcome determination of coefficients a and b at a local scale which weakens the significance of the proposed method as a remote sensing algorithm. Future work will aim to address these issues in an effort to further improve the quality of the presented cloud-sky LST retrieval approach.

Acknowledgements

This work was supported by an Erasmus Mundus Masters Course (G.E.M.) of the European Union as well as the National Natural Science Foundation of China (40971066). The authors thank Dr. Jörg Szarzynski from the University of Bonn, Germany, Dr. Robert Becht from ITC, and their team for sharing data. Thanks also go to the two anonymous reviewers to help us improve this paper.

References

Abu-Hamden, N.H., Reeder, R.C., 2000. Soil thermal conductivity: effects of density, moisture, salt concentration, and organic matter. Soil Science Society of America Journal 64, 1285–1290.

Aires, F., Prigent, C., Rossow, W.B., 2004. Temporal interpolation of global surface skin temperature diurnal cycle over land under clear and cloudy conditions. Journal of Geophysical Research 109, D04313, doi:10.1029/2003JD003527.

Allen, R.G., Pereira, L.S., Raes, D., Smith, M., 1998. Crop evapotranspiration. Guidelines for computing crop water requirements. In: Irrigation and Drainage Paper 56. FAO, Rome, Italy, 86 pp.

Becker, F., Li, Z.L., 1990. Toward a local split window method over land surface. International Journal of Remote Sensing 11, 369–393.

Becker, F., Li, Z.L., 1995. Surface temperature and emissivity at various scales: definition, measurement and related problems. Remote Sensing Reviews 12, 225–253.

Beyer, H.G., Costanzo, C., Heinemann, D., 1996. Modifications of the Heliosat Procedure for irradiance estimates from satellite images. Solar Energy 56 (3), 207–212.

Brümmer, C., Brüggemann, N., Butterbach-Bahl, K., Falk, U., Szarzynski, J., Vielhauer, K., Wassmann, R., Papen, H., 2008. Soil–atmosphere exchange of N_2O and NO in near-natural savanna and agricultural land in Dano, Burkina Faso. Ecosystem 11, 582–600.

Brutsaert, W., 1982. Evaporation into the Atmosphere: Theory, History, and Applications. Kluwer Acad., Norwell, MA, 300 pp.

Coll, C., Caselles, V., 1997. A split-window algorithm for land surfaces temperature from Advanced Very High-Resolution Radiometer data: validation and algorithm comparison. Journal of Geophysical Research 102 (16), 697–716, 713.

Dagestad, K.F., 2004. Mean bias deviation of the Heliosat algorithm for varying cloud properties and sun-ground-satellite geometry. Theoretical and Applied Climatology 79, 215–224.

Dagestad, K.-F., Olseth, J.A., 2007. A modified algorithm for calculating the cloud index. Solar Energy 81, 280–289.

Dai, A.G., Trenberth, K.E., Karl, T.R., 1999. Effects of clouds soil moisture, precipitation, and water vapor on diurnal temperature range. Journal of Climate 12, 2451–2473.

Deardorff, J.W., 1978. Efficient prediction of ground surface temperature and moisture, with inclusion of a layer of vegetation. Journal of Geophysical Research 83, 1889–1903.

Dickinson, R.E, 1988. The force-restore model for surface temperatures and its generalization. Journal Climate 1, 1086–1097.

Ghuman, B.S., Lal, R., 1985. Thermal conductivity, thermal diffusivity, and thermal capacity of some Nigerian soils. Soil Science 139 (1), 74–80.

Gillespie, A., Rokugawa, S., Matsunaga, T., Cothern, S., Hook, S., Kahle, A., 1998. A temperature and emissivity separation algorithm for Advanced Spaceborne Thermal Emission and Reflection radiometer (ASTER) images. IEEE Transactions on Geoscience and Remote Sensing 36, 1113–1126.

Groisman, P.Y., Bardley, R.S., Sun, B.M., 2000. The relationship of cloud cover to near-surface temperature and humidity: comparison of GCM simulations with empirical data. Journal of Climate 13, 1858–1878.

Hammer, A., Heinemann, D., Hoyer, C., Kuhlemann, R., Lorenz, E., Müller, R., Beyer, H.G., 2003. Solar energy assessment using remote sensing technologies. Remote Sensing of Environment 86, 423–432.

Jia, Y.-Y., Tang, B., Zhang, X., Li, Z., 2007. Estimation of land surface temperature and emissivity from AMSR-E data. IEEE Transactions on Geoscience and Remote Sensing, 1849–1852.

Jiménez-Muñoz, J.C., Sobrino, J.A., 2003. A generalized single-channel method for retrieving land-surface temperature from remote sensing data. Journal of Geophysical Research 108 (D22), 4688–4696.

Jin, M.L., 2000. Interpolation of surface radiative temperature measured from polar-orbiting satellites to a diurnal cycle 2. Cloudy-pixel treatment. Journal of Geophysical Research 105 (D3), 4061–4076.
Jin, M.L., Dickinson, R.E., 2002. New observational evidence for global warming from satellite. Geophysical Research Letters 29 (10), 1400, doi:10.1029/2001GL013833.
Katul, G.G., Schieldge, J., Hsieh, C.I., Vidakovic, B., 1998. Skin temperature perturbations induced by surface layer turbulence above a grass surface. Water Resources Research 34 (5), 1265–1274.
Kearney, M., Porter, W.P., 2004. Mapping the fundamental niche: physiology, climate, and the distribution of a nocturnal lizard. Ecology 85 (11), 3119–3131.
Kustas, W.P., Daughtry, C.S.T., van Oevelen, P.J., 1993. Analytical treatment of the relationships between soil heat flux/net radiation ratio and vegetation indices. Remote Sensing of Environment 46, 319–330.
Li, Z.L., Becker, F., 1993. Feasibility of land surface temperature and emissivity determination from AVHRR data. Remote Sensing of Environment 43, 67–85.
Li, Z.Q., Leighton, H.G., Masuda, K., Takashima, T., 1993. Estimation of SW flux absorbed at the surface from TOA reflected flux. Journal of Climate 6, 317–330.
Mallick, K., Bhattacharya, B.K., Chaurasia, S., Dutta, S., Nigam, R., Mukherjee, J., Banerjee, S., Kar, G., Rao, V.U.M., Gadgil, A.S., Parihar, J.S., 2007. Evapotranspiration using MODIS data and limited ground observations over selected agroecosystems in India. International Journal of Remote Sensing 28 (10), 2091–2110.
Mao, K., Shi, J., Li, Z., Qin, Z., Jia, Y., 2005. Land surface temperature and emissivity retrieved from AMSR passive microwave data. IEEE Transactions on Geoscience and Remote Sensing, 2247–2249.
Molineaux, B., Ineichen, P., 1996. On the broad band transmittance of direct irradiance in a cloudless sky and its application to the parameterization of atmospheric turbidity. Solar Energy 56 (6), 553–563.
Möser, W., Raschke, E., 1984. Incident solar radiation over Europe estimated from METEOSAT data. Journal of Climate and Applied Meteorology 23 (1), 166–170.
Nandagiri, L., Kovoor, G.M., 2005. Sensitivity of the Food and Agriculture Organization Penman-Monteith evapotranspiration estimates to alternative procedures for estimation of parameters. Journal of Irrigation and Drainage Engineering 131 (3), 238–248.
Paltridge, G.W., 1974. Global cloud cover and earth surface temperature. Journal of The Atmospheric Sciences 31, 1571–1576.
Peters-Lidard, C.D., Blackburn, E., Liang, X., Wood, E.F., 1998. The effect of soil thermal conductivity parameterization on surface energy fluxes and temperatures. Journal of the Atmospheric Sciences 55, 1209–1224.
Perez, R., Ineichen, P., Moore, K., Kmiecik, M., Chain, C., George, R., Vignola, F., 2002. A new operational model for satellite-derived irradiances: description and validation. Solar Energy 73 (5), 307–317.
Pinker, R.T., Frouin, R., Li, Z., 1995. A review of satellite methods to derive surface shortwave irradiance. Remote Sensing of Environment 51, 108–124.
Qin, Z.H., Zhang, M.H., Arnon, K., Pedro, B., 2001. Mono-window algorithm for retrieving land-surface temperature from Landsat TM 6 data. Acta Geograph Ica Sinica 56 (4), 456–466.
Reginato, R.J., Jackson, R.D., Pinter, P.J.J.R., 1985. Evapotranspiration calculated from remote multispectral and ground station meteorological data. Remote Sensing of Environment 18, 75–89.
Santanello, J.A., Friedl, M.A., 2003. Diurnal covariation in soil heat flux and net radiation. Journal of Applied Meteorology 42, 851–862.
Schneider, S.H., Washington, W.M., Chervin, R.M., 1978. Cloudiness as a climatic feedback mechanism: effects on cloud amounts of prescribed global and regional surface temperature changes in the NCAR GCM. Journal of the Atmospheric Science 35 (12), 2207–2221.
Seguin, B., Becker, F., Phulpin, T., Gu, X.F., Guyot, G., Kerr, Y., King, C., Lagouarde, J.P., Ottlé, C., Stoll, M.P., Tabbagh, A., Vidal, A., 1999. IRSUTE: a minisatellite project for land surface heat flux estimation from field to regional scale. Remote Sensing of Environment 68, 357–369.
Şenkal, O., Kuleli, T., 2009. Estimation of solar radiation over Turkey using artificial neural network and satellite data. Applied Energy 86, 1222–1228.
Sobrino, J.A., Li, Z.L., Stoll, M.P., Becker, F., 1994. Improvements in the split window technique for land surface temperature determination. IEEE Transactions on Geoscience and Remote Sensing 32, 243–253.
Stull, R.B., 1988. An Introduction to Boundary Layer Meteorology. Kluwer Acad., Norwell, MA, 670 pp.
Sun, D.L., Pinker, R.T., 2003. Estimation of land-surface temperature from a geostationary operational environmental satellite (GOES-8). Journal of Geophysical Research 108 (D11), 4326–4341.
Sun, D., Pinker, R.T., 2007. Retrieval of surface temperature from the MSG-SEVIEI observations: Part. Methodology. International Journal of Remote Sensing 28 (23), 5255–5272.
Venus, V., Rugege, D., 2004. Combined use of polar-orbiting and geo-stationary satellites to improve time interpolation in dynamic crop models for food security assessment. In: ISPRS 2004: Proceedings of the XXth ISPRS Congress: Geo-imagery Bridging Continents , 12–23 July 2004, Istanbul, Turkey. Comm. VII PS, WG VII/2, pp. 212–219.
Verstraeten, W.W., Veroustraete, F., Sande, C.J., Grootaers, I., Feyen, J., 2006. Soil moisture retrieval using thermal inertia, determined with visible and thermal spaceborne data, validated for European forests. Remote Sensing of Environment 101, 299–314.
Wan, Z., Dozier, J., 1996. A generalized split-window algorithm for retrieving land surface temperature from space. IEEE Transactions on Geosciences and Remote Sensing 34, 892–905.
Yang, H., Yang, Z.D., 2006. A modified land-surface temperature split window retrieval algorithm and its applications over China. Global and Planetary Change 52, 207–215.
Zhang, R.H., 1996. Experimental Remotely Sensed Model and Ground Foundation. Science Press.